Article

Plume-driven recratonization of deep continental lithospheric mantle

https://doi.org/10.1038/s41586-021-03395-5

Received: 31 March 2020

Accepted: 25 February 2021

Published online: 28 April 2021

Check for updates

Jingao Liu[1,2]✉, D. Graham Pearson[2], Lawrence Hongliang Wang[3], Kathy A. Mather[4], Bruce A. Kjarsgaard[5], Andrew J. Schaeffer[6], Gordon J. Irvine[4], Maya G. Kopylova[7] & John P. Armstrong[8]

Cratons are Earth's ancient continental land masses that remain stable for billions of years. The mantle roots of cratons are renowned as being long-lived, stable features of Earth's continents, but there is also evidence of their disruption in the recent[1–6] and more distant[7–9] past. Despite periods of lithospheric thinning during the Proterozoic and Phanerozoic eons, the lithosphere beneath many cratons seems to always 'heal', returning to a thickness of 150 to 200 kilometres[10–12]; similar lithospheric thicknesses are thought to have existed since Archaean times[3,13–15]. Although numerous studies have focused on the mechanism for lithospheric destruction[2,5,13,16–19], the mechanisms that recratonize the lithosphere beneath cratons and thus sustain them are not well understood. Here we study kimberlite-borne mantle xenoliths and seismology across a transect of the cratonic lithosphere of Arctic Canada, which includes a region affected by the Mackenzie plume event 1.27 billion years ago[20]. We demonstrate the important role of plume upwelling in the destruction and recratonization of roughly 200-kilometre-thick cratonic lithospheric mantle in the northern portion of the Slave craton. Using numerical modelling, we show how new, buoyant melt residues produced by the Mackenzie plume event are captured in a region of thinned lithosphere between two thick cratonic blocks. Our results identify a process by which cratons heal and return to their original lithospheric thickness after substantial disruption of their roots. This process may be widespread in the history of cratons and may contribute to how cratonic mantle becomes a patchwork of mantle peridotites of different age and origin.

Cratons are widely known as repositories for diamonds and metals of economic importance. The ancient ages of lithospheric diamonds[21], along with the prevalence of Archaean melt-depletion ages derived from the roots of cratons[22], indicate that many cratons have been underpinned by deep lithospheric keels since the Archaean eon. Seismology studies clearly indicate the continued presence of thick lithospheric roots beneath most cratons[10–12], suggesting that such keels are an integral part of craton survival. However, despite this apparent stability, there is abundant evidence for cycles of disruption and healing of cratons, for example, in the form of large igneous events that have modified cratons[23]. Despite these disturbances, the thick roots beneath cratons have regrown, and in some cases[23] facilitated diamond growth after healing. Although these examples continue to be documented, indicating that a mechanism for lithospheric healing must exist, the process is not well understood, owing to a lack of direct evidence. We propose a mechanism for rethickening of cratonic lithosphere that has been thinned and disrupted by mantle plumes to repair the thick protective keels beneath the continents. We use direct evidence from kimberlite-borne mantle xenoliths sampled along an Arctic Canada transect, along with geological and seismological evidence. We suggest that this example is a template for the complex evolution of other cratons that have been disrupted and healed by plumes[12,23].

The Slave craton and surrounding areas (Fig. 1a) is an ideal region to examine the cycle of lithospheric thinning and regrowth, owing to its protracted and eventful geological history. The Slave craton assembled during the Meso- to Neoarchaean eras[24], with the presence of Archaean diamonds in kimberlites[25] providing clear evidence of a thick lithospheric keel at that time. The Slave craton subsequently became the upper plate during the Wopmay orogen, with subduction along the entire west side of the craton 1.91–1.70 Gyr ago[26]. This orogenic event also involved the lateral accretion of other depleted cratonic blocks to the north and northwest, which led to the formation and accretion of the roughly 200-km-thick ultradepleted mantle roots beneath Central Victoria Island and Parry Peninsula[27] (Fig. 1a). The subduction involved in the early phases of the Wopmay orogen probably weakened the root of the Slave lithosphere, as a result of metasomatic infiltration of melts and fluids[28,29]. This type of lithospheric preconditioning has been shown to be necessary for effective thermochemical erosion of otherwise buoyant, strong mantle lithosphere by plumes[16,17].

[1]State Key Laboratory of Geological Processes and Mineral Resources, China University of Geosciences (Beijing), Beijing, China. [2]Department of Earth and Atmospheric Sciences, University of Alberta, Edmonton, Alberta, Canada. [3]Department of Environmental Analyses, Institute of Energy Technology, Oslo, Norway. [4]Department of Earth Sciences, Durham University, Durham, UK. [5]Geological Survey of Canada, Ottawa, Ontario, Canada. [6]Geological Survey of Canada, Sidney, British Columbia, Canada. [7]Department of Earth and Ocean Sciences, University of British Columbia, Vancouver, British Columbia, Canada. [8]Lucara Diamond Corp, Vancouver, British Columbia, Canada. ✉e-mail: jingao@cugb.edu.cn

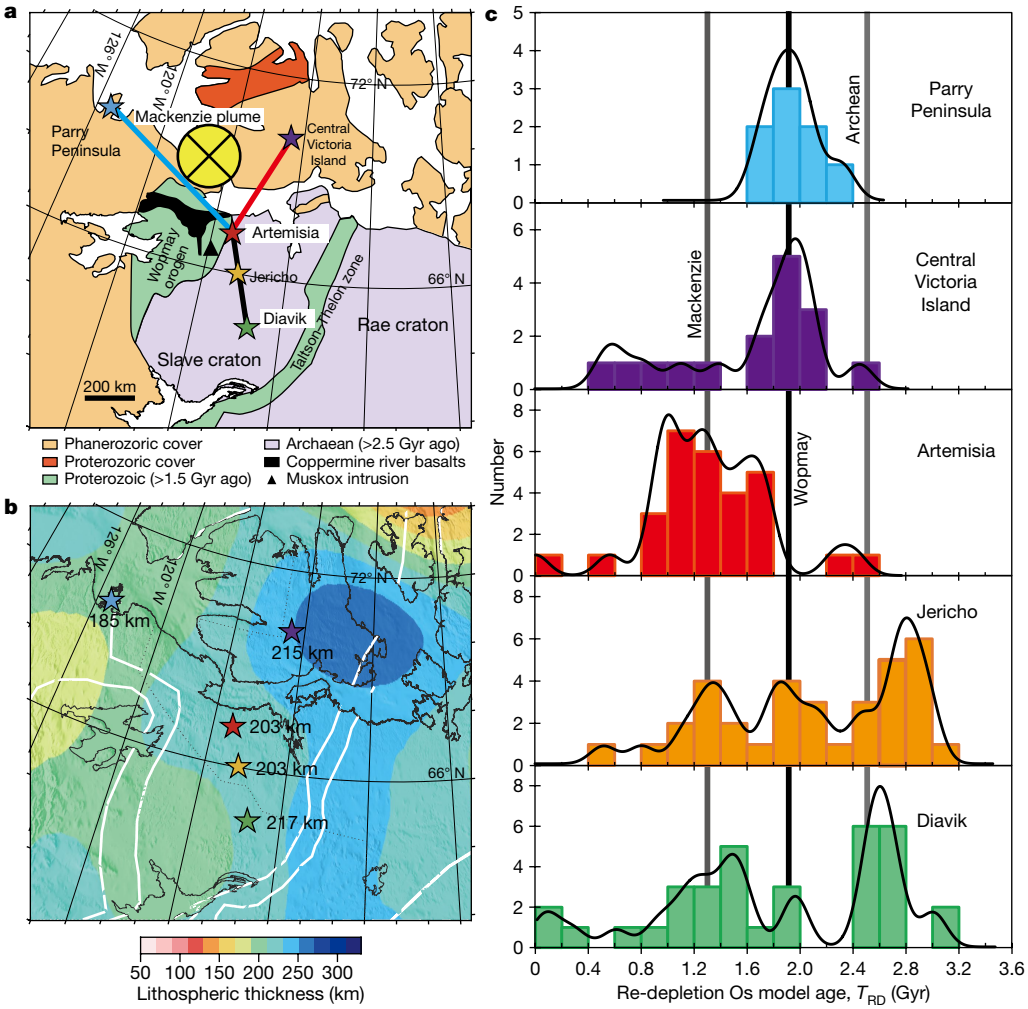


Fig. 1 | Geological map and lithospheric thickness of the Slave craton and surrounding areas, and Os model ages of Slave-craton peridotites. a, Simplified geological map of the Slave craton and surroundings, showing the locations of the kimberlite pipes and peridotite xenoliths (stars) studied, as a transect across the Arctic mantle lithosphere, and the suggested focal point of the Mackenzie plume[31] (yellow crossed circle). Image adapted with permission from ref. [46], Minister of Natural Resources Canada, GeoScienceWorld. **b**, Map of the depth of the lithosphere–asthenosphere boundary computed from SL2013NA[12] using the method of ref. [47]. Colours indicate depth of the seismic estimate to the base of the thermal lithosphere–asthenosphere boundary. White lines denote the boundaries of the Archaean and Palaeoproterozoic tectonic domains. Kimberlite pipes denoted as in **a**, with the lithospheric thickness determined by palaeogeotherms at the time of kimberlite eruption (Extended Data Fig. 3, Methods). **c**, Histograms and probability density functions (black curves) of Re-depletion Os model age (T_{RD}) of peridotites from the Slave craton. Data are provided in Supplementary Table 1. Also shown are key geological events (vertical black and grey bars) throughout the history of the Slave craton.

Despite the assembly of this extensive ancient crustal domain that is underlain by thick diamondiferous mantle roots, in Mesoproterozoic times, this area became the focus of one of Earth's largest flood-basalt magmatic events—the 1.27-Gyr-old Mackenzie large igneous province[20]. The production of the voluminous tholeiitic magmas associated with this event required mantle upwelling beneath lithosphere that was no greater than 80 km thick in the axis of melt production[30,31]. However, present-day seismology models define the presence of a roughly 200-km-thick lithospheric root coupled with high seismic velocity throughout the entire region[12] (Fig. 1b, Extended Data Fig. 1a). This sequence of events requires a history in which the thinning that enabled the production of the very extensive Mesoproterozoic large igneous province must have transitioned to a regime of lithospheric underplating and thickening. We examine the geological, geochronological and geochemical evidence using kimberlite-derived mantle xenoliths and xenocrysts as probes of the lithospheric history. We explore the mechanism for lithospheric healing by using geodynamic models to determine the fate of plume-derived residual mantle in a lithospheric thin spot between two thicker cratonic blocks.

Mantle keels beneath Arctic Canada

Kimberlite-borne mantle peridotites across the Slave craton, from its centre (Diavik), through Jericho to the northern Slave (Artemisia), and extending to the north (Central Victoria Island) and northwest (Parry Peninsula; Fig. 1a), all have similarly low alumina contents, indicative of extensive melt depletion and akin to typical global cratonic mantle values (Extended Data Fig. 2). We used pressure–temperature determinations on mineral pairs from mantle xenoliths and from Cr-diopside grains (Methods) to construct palaeogeotherms, following an existing approach[32]. In some cases, equilibration temperatures were calculated from Ni-in-garnet thermometry, which also shows elevated temperatures consistent with derivation from depths of up to about 200 km. These data reveal the existence of a thick lithospheric mantle root (about 200 km) beneath the entire region between about 616 Myr and 50 Myr ago—the times of kimberlite sampling (Extended Data Fig. 3; see Methods for details)—consistent with the diamondiferous nature of the host kimberlites. Such thick lithosphere is also in agreement with present-day seismic

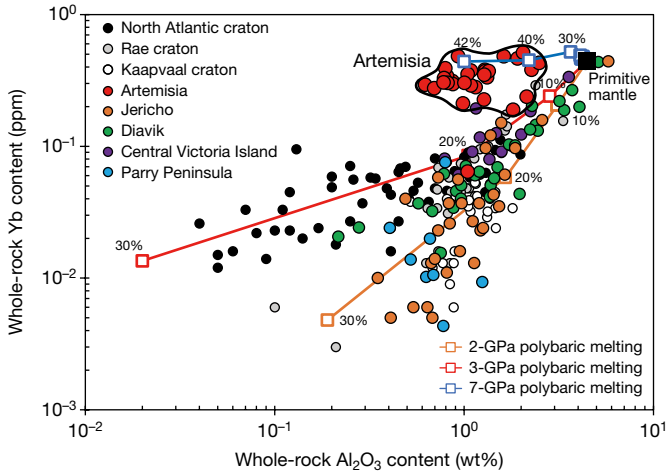


Fig. 2 | Whole-rock Yb versus Al_2O_3 content for Slave peridotites. Curves show the trajectories of residual mantle after polybaric fractional melting, beginning at 2 GPa (spinel facies; orange squares), 3 GPa (shallow garnet facies; red squares) and 7 GPa (deep garnet facies; blue squares). The partial melting calculations followed those in ref. [39], supplementary material C. Unlike all other cratonic peridotites, the very high Yb (heavy rare-earth element) abundances of Artemisia peridotites clearly indicate initial melting in the presence of high modal garnet, that is, ultradeep plume melting. Previously published data from the North Atlantic, Rae and Kaapvaal cratons[39] (circles) are plotted for comparison.

observations (Fig. 1b), demonstrating that the lithosphere has remained thick through the Phanerozoic.

There is a clearly defined north–south variation in the modes in Re-depletion Os model age (T_{RD}) in the Slave craton peridotites (Fig. 1c). The relative fraction of Slave-craton Archaean model ages decreases as the fraction of Mesoproterozoic model ages increases, with the latter being higher in the northern Slave. Given the refractory nature of the peridotites, neither melt refertilization nor sulfur-saturated melt metasomatism is a viable means to reset the Re–Os isotope system of the cratonic lithospheric mantle[33]. Therefore, T_{RD} for refractory peridotites reflects their formation age. Similarly to many other Archaean cratonic regions[34], T_{RD} for central Slave mantle is predominantly Meso–Neoarchaean, marking the time of the formation of cratonic lithospheric mantle root[22,35].

Progressing northward in the Slave craton from Diavik to Artemisia, the lithospheric mantle peridotites from each location show a decreasing proportion of Archaean T_{RD} complemented by an increasing proportion of Palaeoproterozoic and Mesoproterozoic T_{RD} (Fig. 1c). Further north, no Archaean T_{RD} appear in the Central Victoria Island and Parry Peninsula peridotites, which are dominated by Palaeoproterozoic T_{RD} (about 2.0 Gyr ago)[27]. The peridotites from Artemisia (northern Slave craton) are characterized by a peak in T_{RD} corresponding to the Mesoproterozoic (about 1.3 Gyr ago); Fig. 1c). By contrast, progressing south, the mantle beneath Jericho and Diavik shows diminished Mesoproterozoic signatures but a persistent minor T_{RD} peak corresponding to the Palaeoproterozoic (1.8 Gyr ago; Fig. 1c). The presence of the latter peak probably reflects newly formed lithospheric mantle added during the Wopmay subduction and accretionary orogen, mirroring the creation of new cratonic lithosphere further north and northwest (beneath Victoria Island and the Parry Peninsula) associated with the assembly of the Laurentia supercontinent[27].

Plume-driven asymmetric mantle erosion

No prominent signature at T_{RD} = 1.8 Gyr (Wopmay age) is present in the lithosphere beneath Artemisia, in the northern Slave craton. Preconditioning of the lithosphere is necessary to weaken it before erosion by plumes, because refractory cratonic lithosphere is essentially immune to major plume erosion[17]. Hence, our finding suggests that the Artemisia lithospheric mantle was weakened by metasomatic activity due to fluid or melt from Wopmay subduction and subsequently eroded by the impact of the major Mesoproterozoic Mackenzie plume (1.27 Gyr ago[20]). The resulting Muskox intrusion and the Coppermine flood basalts are the surface expression of this plume[20,36] (Fig. 1a); the comagmatic Mackenzie dyke swarm penetrated the entirety of the Slave craton, extending far beyond it (about 2,400 km), into more distal areas of the Canadian Shield. The interpreted focal point of the Mackenzie plume head is around 350 km northwest of the Artemisia kimberlite[31] (Fig. 1a). Magma flow in the Mackenzie dykes changes from mostly vertical to mostly horizontal about 550 km from the focal point of the plume[31]. Artemisia lies within the vertical flow region, suggesting that tholeiitic magmas in this region were vertically traversing thin lithosphere at the time of their eruption. Basaltic melts of this chemical composition require that the lithosphere was no thicker than 80 km at this time[30]. By contrast, Mackenzie dykes traversing the lithosphere in the Jericho and central Slave localities are within the horizontal flow regime, suggesting lateral magma flow within the crust and removing the requirement for thinned lithosphere. Combined with the north–south distribution of T_{RD} = 1.3 Gyr at Artemisia, Jericho and Diavik (Fig. 1c), these observations imply that magmatic processes associated with the Mackenzie event had a lesser effect on the lithosphere beneath Jericho than on that beneath Artemisia, waning further to the south at Diavik in the centre of the craton. In addition to mantle peridotite xenoliths, the Artemisia kimberlite contains an unusually high volume of crustal xenoliths of Mackenzie dolerites and gabbros, much higher than in kimberlites further south, indicative of the intense Mackenzie-age influx of basaltic magma through the lithosphere at this location. The voluminous vertical magma flow in tholeiitic dykes that forms the intense Mackenzie-dyke swarm in the northern Slave craton, together with the formation of the coeval and voluminous Muskox intrusion and Coppermine basalts (Fig. 1a), requires substantial lithospheric erosion and thinning in this region; this is achieved by the Mackenzie plume removing lithosphere. The resulting lithospheric thin spot allowed the production of large volumes of plume-related melt via increased plume upwelling, a process focused at the margins of cratons[37].

Mantle lithosphere to the south of Artemisia, coupled with the absence of any significant T_{RD} = 1.3 Gyr at Central Victoria Island and Parry Peninsula, clearly indicates little or minor influence by the Mackenzie plume beneath these regions. Central Victoria Island, Parry Peninsula and Artemisia all lie at similar distances (about 350 km) from the focal point of the Mackenzie plume, suggesting asymmetric lithospheric erosion to the south of the plume head, which follows the strike of the larger and higher-density areas of Mackenzie dykes. This is supported by the small but non-zero gradient in seismic velocity observed trending north–northwest from Artemisia through to west of Victoria Island (Extended Data Fig. 1b). The occurrence of Coppermine basalts and Muskox intrusion proximal to and west–southwest of Artemisia (Fig. 1a) is also consistent with asymmetric lithospheric erosion.

Plume-driven recratonization

During Mackenzie-plume-induced rifting, a lithospheric thin spot developed between the roughly 200-km-thick Slave craton to the south and the roughly 200-km-thick mantle roots below Central Victoria Island to the north and the Parry Peninsula to the northwest (Extended Data Fig. 3). This allowed melt to be produced and created a trap for upwelling, buoyant and strong residues from plume melting. This basal lithospheric topography, coupled with plume melting, created a situation where the thin spot healed via the vertical accretion of melting residues (peridotite). We evaluate this hypothesis using geochemistry and geodynamic modelling.

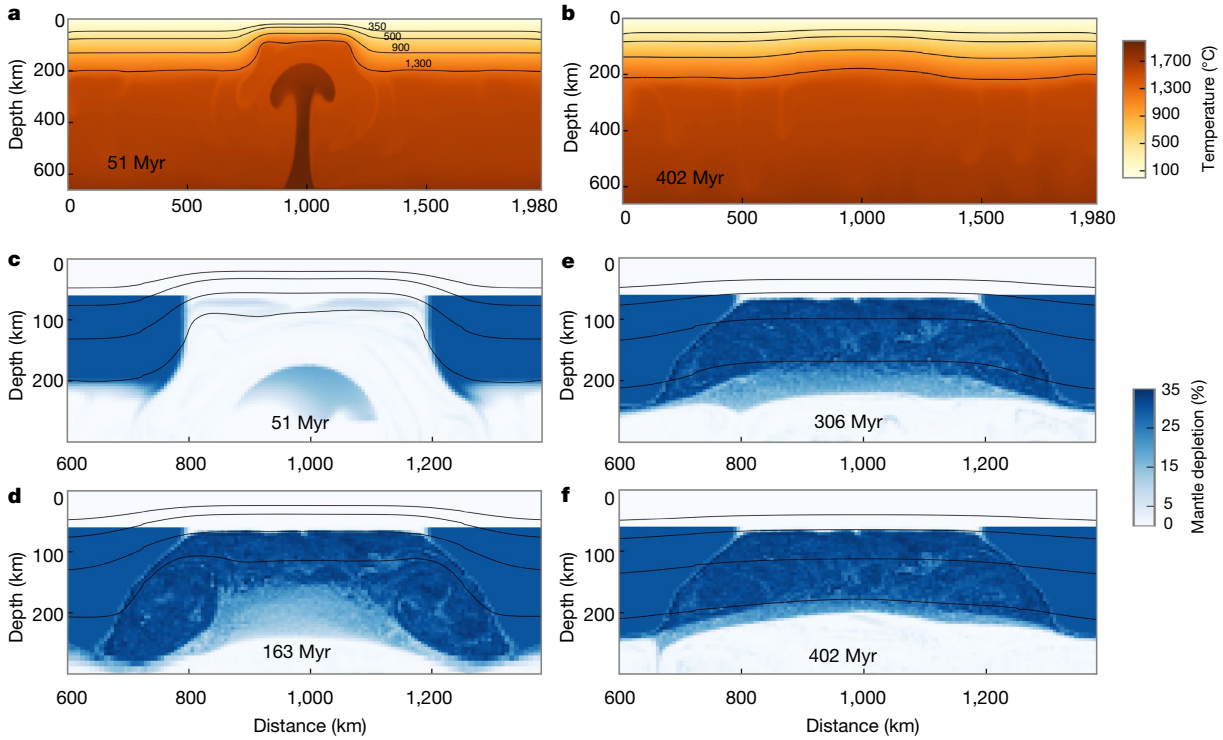


Fig. 3 | Numerical modelling of plume residues filling a thin spot between thick cratonic lithospheric roots. a, **b**, Temperature field (colour scale, contours) showing initial plume upwelling 51 Myr (**a**; corresponding to the formation of the Mackenzie large igneous province 1,267 Myr ago) and 402 Myr (**b**; 916 Myr ago in the geological record) after the start of the model. **c**–**f**, Combined compositional fields for plume residue and cratonic root (colour scale) 51 Myr (**c**; 1,267 Myr ago), 163 Myr (**d**; 1,155 Myr ago), 306 Myr (**e**; 1,020 Myr ago) and 402 Myr (**f**; 916 Myr ago) after the start of the model. The cratonic root shallower than 60 km is not plotted. The black contours indicate the temperature, as in **a** and **b**. For simplicity, we assume that the initial cratonic root is 35% melt-depleted everywhere. The lithosphere beneath the thin spot grows to roughly 200 km depth through infilling by buoyant plume residues. Details of the modelling are provided in Methods and Extended Data Figs. 6–8, which demonstrate the rethickening and recratonization of the lithospheric thin spot by plume residues.

The lithosphere beneath Artemisia must have healed close to its original thickness by 616 Myr ago, because the kimberlite that erupted at this time sampled diamonds and deeply derived lithospheric peridotite xenoliths. The origin of this peridotite, in terms of its depth of melt extraction and likely geodynamic environment, may be tested by using geochemistry. In our proposed model, many of the Mesoproterozoic peridotites should bear the signature of deep melting with garnet present as a residual phase. Although mantle peridotite xenoliths ubiquitously record modification by subsequent metasomatic events, as reflected by enrichments of melt- and/or fluid-mobile elements[35] (Extended Data Fig. 4), the heavy rare-earth elements (for example, Yb and Lu) remain relatively resistant to alteration and metasomatism. Being partitioned differently into residual garnet and spinel during melting, these elements may be used to estimate the original depths of partial mantle melting[38,39]. The peridotites from Diavik, Jericho, Parry Peninsula and Central Victoria Island all have similarly low Lu and Yb contents typical of global cratonic peridotites, with a few having higher Lu and Yb contents similar to estimates for primitive mantle (Fig. 2). Combined with a melt-depletion indicator—peridotite Al_2O_3 content—these residual mantle rocks are explained by variable degrees of relatively shallow mantle melting[13,39] (Fig. 2). However, despite having similar major-element contents to the other Slave peridotites (for example, Al_2O_3; Extended Data Fig. 2), the Artemisia peridotites have much higher Lu and Yb contents at a given Al content; and these elemental systematics are different from those of other cratonic peridotites (Fig. 2, Extended Data Fig. 5). The observed Lu and Yb enrichment is unlikely to be due to metasomatism, because kimberlites and related deep-sourced melts have the lowest abundances of heavy rare-earth elements of any mantle-derived melts. Modelling indicates that only high-degree, high-pressure mantle melting, with garnet stable for much of the melting interval, can account for the Al and heavy rare-earth element systematics for Artemisia (Fig. 2, Extended Data Fig. 5). The data are consistent with the majority of Artemisia peridotites being in equilibrium with garnet as a residual phase throughout the melting interval, whereas a minor subset melted beyond the point of garnet stability, allowing Lu and Yb concentrations to decrease as a result of the absence of a residual phase that strongly prefers heavy rare-earth elements. The Artemisia peridotites provide clear evidence for an origin for plume-derived melt residues that involves extensive melt being extracted at high pressure.

To determine how effective melting residues of plumes are at infilling lithospheric thin spots, we conducted numerical modelling of plume upwelling on a thinned lithospheric mantle situated between two thick cratonic blocks (Methods). The modelling results show that mantle plumes are able to fill the thin lithospheric trap, via upwelling of highly melt-depleted, high-pressure mantle residues[40] (Fig. 3, Extended Data Figs. 6–8) due to the buoyant, rheologically strong nature of residual peridotites compared to unmelted mantle. Buoyant melt residues are drawn into the lithospheric thin spot irrespective of whether the upwelling is directly beneath the thin lithosphere or displaced laterally from it. Through this process, the lithosphere recovers at least 90% of its original thickness when combined with cooling over a period of about 300 Myr (Extended Data Fig. 8). The newly accreted lithosphere has long-term stability due to its high viscosity and buoyancy. Hence, we conclude that mantle plumes may not only destroy the metasomatized cratonic mantle root if it is sufficiently preweakened[16–18], but also subsequently heal the root to approximately its original thickness using newly formed, buoyant, deep melting residues of plumes. The geodynamic modelling also indicates that some fragments of cratonic peridotites adjacent to the lithospheric trap are incorporated into the newly formed lithospheric mantle (Extended Data Fig. 6), consistent

with the observed, yet volumetrically minor, Archaean–early Palaeoproterozoic fragments in the Artemisia mantle xenoliths (Fig. 1c, Extended Data Fig. 9).

Although there are subtle differences in trace-element chemistry (heavy rare-earth elements), the major-element composition of the Artemisia plume-derived peridotites is similar to that of other Slave cratonic peridotites and is reflected in the generally comparable seismic-velocity signature of the Artemisia region relative to surrounding areas (Fig. 1b, Extended Data Fig. 1). We find that Artemisia lies within a region characterized by shorter-scale lateral variations in seismic velocity (Extended Data Fig. 1b), which suggests the presence of a different mantle domain, as expected.

It is clear from the geological record that cratonic lithosphere goes through cycles of thinning and rethickening. Studies of mantle xenoliths and diamonds have shown that the midcontinent rift event 1.1 Gyr ago thinned the lithosphere of the Superior craton, which then subsequently regrew to be thick enough to be mineralized by Neoproterozoic diamonds[23,41], recratonizing this region. Another example of coupled erosion and recratonization processes is the 2.05-Gyr-old Bushveld complex. The lithosphere of the Kaapvaal craton was thinned enough to generate the voluminous basaltic melt of the Bushveld complex 2.0 Gyr ago and of the Umkondo large igneous event 1.1 Gyr ago[42]. Yet, seismic studies indicate that the craton lithosphere is now around 200 km thick[7]. Similar scenarios have occurred for most other surviving cratons, which have restored close to their original lithospheric thickness following substantial disruption (causing voluminous basaltic melt) of their lithosphere roots by Proterozoic mantle plumes (Extended Data Table 1). A clear implication of this cycle of lithospheric thinning and rethickening is that cratonic roots are a patchwork of peridotites of different ages and origins, created by cratonic assembly and subsequent modification[13,15,16,22,30], as illustrated by, for example, the Kaapvaal[43] and Rae[44] cratons. This is consistent with the variable T_{RD} spectra seen in global cratonic peridotites[22] and their compositional variability[14,22,45]. The Slave craton lithospheric transect observed here may be a template for the complex evolution of other cratons.

Online content

Any methods, additional references, Nature Research reporting summaries, source data, extended data, supplementary information, acknowledgements, peer review information; details of author contributions and competing interests; and statements of data and code availability are available at https://doi.org/10.1038/s41586-021-03395-5.

1. Menzies, M. A., Fan, W.-M. & Zhang, M. in *Magmatic Processes and Plate Tectonics* (eds Prichard, H. M. et al.) 71–81 (Geological Society, 1993).
2. Griffin, W. L., Zhang, A. D., O'Reilly, S. Y. & Ryan, C. G. in *Mantle Dynamics and Plate Interactions in East Asia* (eds Flower, M. et al.) 107–126 (American Geophysical Union, 1998).
3. Griffin, W. L. et al. The origin and evolution of Archean lithospheric mantle. *Precambr. Res.* **127**, 19–41 (2003).
4. Carlson, R. W., Irving, A. J., Schulze, D. J. & Hearn, B. C. Timing of Precambrian melt depletion and Phanerozoic refertilization events in the lithospheric mantle of the Wyoming Craton and adjacent Central Plains Orogen. *Lithos* **77**, 453–472 (2004).
5. Peace, A., Foulger, G., Schiffer, C. & McCaffrey, K. Evolution of Labrador Sea- Baffin Bay: plate or plume processes? *Geosci. Can.* **44**, 91–102 (2017).
6. Kopylova, M. G., Tso, E., Ma, F., Liu, J. & Pearson, D. G. The Metasomatized Mantle beneath the North Atlantic Craton: insights from Peridotite Xenoliths of the Chidliak Kimberlite Province (NE Canada). *J. Petrol.* **60**, 1991–2024 (2019).
7. James, D. E., Fouch, M. J., VanDecar, J. C., van der Lee, S. & Group, K. S. Tectospheric structure beneath southern Africa. *Geophys. Res. Lett.* **28**, 2485–2488 (2001).
8. Hanson, R. E. et al. Coeval large-scale magmatism in the Kalahari and Laurentian cratons during Rodinia assembly. *Science* **304**, 1126–1129 (2004).
9. Ernst, R. E., Wingate, M. T. D., Buchan, K. L. & Li, Z. X. Global record of 1600–700Ma Large Igneous Provinces (LIPs): implications for the reconstruction of the proposed Nuna (Columbia) and Rodinia supercontinents. *Precambr. Res.* **160**, 159–178 (2008).
10. James, D. E. & Fouch, M. J. Formation and evolution of Archaean cratons: insights from southern Africa. *Geol. Soc. Lond. Spec. Publ.* **199**, 1–26 (2002).
11. Snyder, D. B., Humphreys, E. & Pearson, D. G. Construction and destruction of some North American cratons. *Tectonophysics* **694**, 464–485 (2017).
12. Schaeffer, A. J. & Lebedev, S. Imaging the North American continent using waveform inversion of global and USArray data. *Earth Planet. Sci. Lett.* **402**, 26–41 (2014).
13. Lee, C.-T. A., Luffi, P. & Chin, E. J. Building and destroying continental mantle. *Annu. Rev. Earth Planet. Sci.* **39**, 59–90 (2011).
14. Aulbach, S. Craton nucleation and formation of thick lithospheric roots. *Lithos* **149**, 16–30 (2012).
15. Perchuk, A. L., Gerya, T. V., Zakharov, V. S. & Griffin, W. L. Building cratonic keels in Precambrian plate tectonics. *Nature* **586**, 395–401 (2020).
16. Foley, S. F. Rejuvenation and erosion of the cratonic lithosphere. *Nat. Geosci.* **1**, 503–510 (2008).
17. Wang, H., van Hunen, J. & Pearson, D. G. The thinning of subcontinental lithosphere: the roles of plume impact and metasomatic weakening. *Geochem. Geophys. Geosyst.* **16**, 1156–1171 (2015).
18. Hu, J. et al. Modification of the Western Gondwana craton by plume–lithosphere interaction. *Nat. Geosci.* **11**, 203–210 (2018); publisher correction **11**, 544 (2018).
19. Wu, F.-Y., Yang, J.-H., Xu, Y.-G., Wilde, S. A. & Walker, R. J. Destruction of the North China Craton in the Mesozoic. *Annu. Rev. Earth Planet. Sci.* **47**, 173–195 (2019).
20. LeCheminant, A. N. & Heaman, L. M. Mackenzie igneous events, Canada: middle Proterozoic hotspot magmatism associated with ocean opening. *Earth Planet. Sci. Lett.* **96**, 38–48 (1989).
21. Shirey, S. et al. in *Deep Mantle Carbon Evolution from the Diamond Record* (eds Orcutt, B. N. et. al) Ch. 5, 89–128 (Cambridge Univ. Press, 2019).
22. Pearson, D. G. & Wittig, N. in *Treatise of Geochemistry* 2nd edn, Vol. 3, (Holland, H. D. & Turekian, K. K.) Ch. 3.6, 255–292 (Elsevier, 2014).
23. Smit, K. V., Pearson, D. G., Stachel, T. & Seller, M. Peridotites from Attawapiskat, Canada: Mesoproterozoic reworking of Palaeoarchaean lithospheric mantle beneath the northern Superior Superterrane. *J. Petrol.* **55**, 1829–1863 (2014).
24. Bleeker, W. Archaean tectonics: a review, with illustrations from the Slave craton. *Geol. Soc. Spec. Publ.* **199**, 151–181 (2002).
25. Westerlund, K. J. et al. A subduction wedge origin for Paleoarchean peridotitic diamonds and harzburgites from the Panda kimberlite, Slave craton: evidence from Re–Os isotope systematics. *Contrib. Mineral. Petrol.* **152**, 275 (2006).
26. Hoffman, P. F. United plates of America, the birth of a craton: early Proterozoic assembly and growth of Laurentia. *Annu. Rev. Earth Planet. Sci.* **16**, 543–603 (1988).
27. Liu, J. et al. Diamondiferous Paleoproterozoic mantle roots beneath Arctic Canada: a study of mantle xenoliths from Parry Peninsula and Central Victoria Island. *Geochim. Cosmochim. Acta* **239**, 284–311 (2018).
28. Schmidberger, S. S. et al. Lu–Hf, in-situ Sr and Pb isotope and trace element systematics for mantle eclogites from the Diavik diamond mine: evidence for Paleoproterozoic subduction beneath the Slave craton, Canada. *Earth Planet. Sci. Lett.* **254**, 55–68 (2007).
29. Ootes, L. et al. Pyroxenitic magma conduits (ca. 1.86 Ga) in Wopmay orogen and Slave craton: petrogenetic constraints from whole rock and mineral chemistry. *Lithos* **354–355**, 105220 (2020).
30. McKenzie, D. & Bickle, M. J. The volume and composition of melt generated by extension of the lithosphere. *J. Petrol.* **29**, 625–679 (1988).
31. Ernst, R. E. & Baragar, W. R. A. Evidence from magnetic fabric for the flow pattern of magma in the Mackenzie giant radiating dyke swarm. *Nature* **356**, 511–513 (1992).
32. Mather, K. A., Pearson, D. G., McKenzie, D., Kjarsgaard, B. A. & Priestley, K. Constraints on the depth and thermal history of cratonic lithosphere from peridotite xenoliths, xenocrysts and seismology. *Lithos* **125**, 729–742 (2011).
33. Rudnick, R. L. & Walker, R. J. Interpreting ages from Re-Os isotopes in peridotites. *Lithos* **112**, 1083–1095 (2009).
34. Aulbach, S. et al. Mantle formation and evolution, Slave Craton: constraints from HSE abundances and Re–Os isotope systematics of sulfide inclusions in mantle xenocrysts. *Chem. Geol.* **208**, 61–88 (2004).
35. Pearson, D. G., Canil, D. & Shirey, S. B. in *Treatise of Geochemistry* 2nd edn, Vol. 3 (Holland, H. D. & Turekian, K. K.) Ch. 3.5, 169–253 (Elsevier, 2014).
36. Day, J. M. D., Pearson, D. G. & Hulbert, L. J. Rhenium-osmium isotope and platinum-group element constraints on the origin and evolution of the 1.27 Ga Muskox layered intrusion. *J. Petrol.* **49**, 1255–1295 (2008).
37. Thompson, R. N. & Gibson, S. A. Subcontinental mantle plumes, hotspots and pre-existing thinspots. *J. Geol. Soc. Lond.* **148**, 973–977 (1991).
38. Stachel, T., Viljoen, K. S., Brey, G. & Harris, J. W. Metasomatic processes in lherzolitic and harzburgitic domains of diamondiferous lithospheric mantle: REE in garnets from xenoliths and inclusions in diamonds. *Earth Planet. Sci. Lett.* **159**, 1–12 (1998).
39. Wittig, N. et al. Origin of cratonic lithospheric mantle roots: a geochemical study of peridotites from the North Atlantic Craton, West Greenland. *Earth Planet. Sci. Lett.* **274**, 24–33 (2008).
40. Sleep, N. H. Lateral flow and ponding of starting plume material. *J. Geophys. Res. Solid Earth* **102**, 10001–10012 (1997).
41. Stachel, T. et al. The Victor Mine (Superior Craton, Canada): Neoproterozoic lherzolitic diamonds from a thermally-modified cratonic root. *Mineral. Petrol.* **112**, 325–336 (2018).
42. Hanson, R. E., Martin, M. W., Bowring, S. A. & Munyanyiwa, H. U-Pb zircon age for the Umkondo dolerites, eastern Zimbabwe: 1.1 Ga large igneous province in southern Africa–East Antarctica and possible Rodinia correlations. *Geology* **26**, 1143–1146 (1998).
43. Carlson, R. W., Pearson, D. G. & James, D. E. Physical, chemical, and chronological characteristics of continental mantle. *Rev. Geophys.* **43**, RG1001 (2005).
44. Liu, J. et al. Age and evolution of the deep continental root beneath the central Rae craton, northern Canada. *Precambr. Res.* **272**, 168–184 (2016).
45. Griffin, W. L., O'Reilly, S. Y., Afonso, J. C. & Begg, G. C. The composition and evolution of lithospheric mantle: a re-evaluation and its tectonic implications. *J. Petrol.* **50**, 1185–1204 (2009).
46. Kjarsgaard, B. A. in *Decade of North American Geology* Vol. P1 (eds Eckstrand, O. R. et al.) 557–566 (Geological Survey of Canada, 1995).
47. Steinberger, B. & Becker, T. W. A comparison of lithospheric thickness models. *Tectonophysics* **746**, 325–338 (2018).

Publisher's note Springer Nature remains neutral with regard to jurisdictional claims in published maps and institutional affiliations.

© The Author(s), under exclusive licence to Springer Nature Limited 2021

Methods

Samples

The samples examined in this study are 127 kimberlite-borne peridotite mantle xenoliths from five localities, including the central Slave (Diavik, with eruption age of about 55 Myr[48]), through Jericho (eruption age of 172 Myr[49]) to the northern Slave (Artemisia, with eruption age of about 616 Myr[50]), as well as the area further north of the Slave craton (Central Victoria Island and Parry Peninsula, both erupted roughly 270 Myr ago[51]; Fig. 1). We analysed whole-rock major- and trace-element contents and Re–Os isotope compositions for 34 peridotites from Diavik and 30 from Artemisia. Moreover, we analysed Re–Os isotope composition for 36 peridotites from Jericho (data for whole-rock major-element contents[52] and analyses of whole-rock trace-element contents[39] were reported previously). In addition, we analysed whole-rock trace-element contents for 17 peridotites from Central Victoria Island and 10 from Parry Peninsula (data of whole-rock major-element contents and Re–Os isotope compositions were reported previously[27]). Major-element contents of mineral phases from xenoliths and concentrates were determined for samples from Diavik, Jericho and Artemisia; those from Central Victoria Island and Parry Peninsula were reported previously[27].

Whole-rock major-element analysis

Whole-rock powders were made from kimberlite contamination-free mantle xenoliths using an automated agate or alumina ball mill or by hand using an agate mortar and pestle. Whole-rock major-element compositions were determined by X-ray fluorescence on fused glass disks made from these whole-rock powders (see ref. [53] for detailed protocols) at the Open University, UK (for Diavik and Artemisia peridotites), or at Franklin and Marshall College, USA (for Central Victoria Island and Parry Peninsula peridotites), and are provided in Supplementary Table 1. Analytical precision and accuracy were estimated to be typically better than 1% for major-element oxides with concentrations of more than 0.5%, and better than 5% for the remaining major and minor elements, as demonstrated by data determined for the international reference rocks (for example, WS-E, G94, UB-N and MUH-1; Supplementary Table 2). The Jericho peridotites were measured previously at the Geochemical Lab of McGill University (Montreal, Canada)[52]. Because mantle peridotites have experienced serpentinization, silicification and/or carbonation to different extents, we carried out a series of calculations and normalization following the method of ref. [44] to retrieve the anhydrous pristine major-element compositions of these rocks (Supplementary Table 1; box-and-whisker plot of the normalized whole-rock anhydrous Al_2O_3 contents is shown in Extended Data Fig. 2).

Whole-rock trace-element analysis

Whole-rock trace elements were analysed following previously reported protocols[27] at the China University of Geosciences (Beijing) for samples from Diavik, Artemisia, Central Victoria Island and Parry Peninsula and for some replicate Artemisia samples at the China University of Geosciences (Wuhan); the data are provided in Supplementary Table 1. Analyses of international rock standards are listed in Supplementary Table 3. Trace-element data of the Jericho whole-rock peridotites were taken at Durham University and were reported previously[39]. Digestion and dilution procedures are described elsewhere[54]. The chondrite-normalized rare-earth-element patterns of these peridotites are shown in Extended Data Fig. 4.

Mineral major-element analysis

Mineral major-element mineral analysis was performed using a CAMECA SX100 or a JEOL 8900R electron microprobe at the University of Alberta, the University of Cambridge, UK, or the Saskatchewan Research Council, and are provided in Supplementary Table 4. In general, three points were analysed in the core of each crystal to produce an average composition, and one point was analysed on the rim of each crystal to assess variability from core to rim. Various natural minerals (silicate and oxide) were used for standardization. Data reduction was performed using a ZAF correction (where Z is the atomic number correction, A is the absorption correction and F is the fluorescence correction).

Garnet trace-element analysis

Garnet trace-element analysis was acquired by laser-ablation inductively coupled plasma mass spectrometry (LA-ICP-MS) at the Geological Survey of Canada. The methods are as described elsewhere[44]. Three analyses were performed on the cores of individual garnets to produce an average composition. The data are provided in Supplementary Table 5. Nickel-in-garnet equilibrium temperatures were calculated and are provided in Supplementary Table 5.

Whole-rock Re–Os isotope analysis

Re–Os isotopic compositions were determined using an isotope dilution technique coupled with high-pressure Asher (HPA-S, Anton Paar) or Carius tube digestion at the University of Alberta for samples from Central Victoria Island and Parry Peninsula[27] and at Durham University for samples from Diavik, Jericho and Artemisia; all data are provided in Supplementary Table 1. About 1 g of whole-rock powder, in combination with an appropriate amount of mixed ^{185}Re–^{190}Os spikes, was attacked by inverse Aqua Regia in an HPA-S (130 bar) for about 16 h at about 290 °C or in a Carius tube for 4 days at about 240 °C. Os was processed by solvent extraction followed by microdistillation. Re was separated and purified using cation exchange chromatography followed by BPHA solvent extraction at the University of Alberta[55] or using anion exchange chromatography at Durham University[56].

Os isotope ratios were measured as OsO_3^- using peak-hopping scanning electron microscopy (SEM) or using static multiple Faraday collectors and amplifiers equipped with 10^{12}-Ω resistors by a Thermo Scientific Triton Plus thermal ionization mass spectrometer at the University of Alberta[57]. Os reference materials of both the University of Maryland Johnson Matthey Os Standard and DROsS were analysed to meet within 0.02% of the accepted values[58]. Re cuts were measured via peak-hopping SEM on a Thermo Element 2 XR ICP-MS at the University of Alberta or at Durham University. The Beni Bousera peridotite GP-13 was used as our in-house reference material, and the results agree well with accepted values (see data in ref. [27]). During the analytical campaign, four total procedural blanks were measured: $^{187}Os/^{188}Os = 0.174 \pm 0.018$, 1.0 ± 0.7 pg Os and 4.2 ± 2.2 pg Re. All data were corrected for average blanks.

Palaeogeotherms

The single-grain clinopyroxene thermobarometer (using the compositional screens recommended by ref. [59]), on clinopyroxene derived from xenoliths or coarse concentrates from local till sampling, was used to construct the palaeogeotherm at the time of eruption for each locality. Palaeogeotherms were fitted to the pressure–temperature data using a previously documented procedure[32] (Extended Data Fig. 3; fitting parameters are provided in Extended Data Table 2; pressure–temperature data are provided in Supplementary Table 6). The Diavik data ($n = 65$) define a palaeogeotherm that is similar to that determined previously for the central Slave craton from ref. [59], which corresponds to a lithosphere thickness of 217 ± 21 km, whereas the Jericho data ($n = 39$) produce a similar geotherm to a lithosphere thickness of 203 ± 11 km (Extended Data Fig. 3). Data for Parry Peninsula xenolith and concentrate clinopyroxene grains ($n = 362$) generate a palaeogeotherm with a lithosphere thickness of 185 ± 20 km (Extended Data Fig. 3)[27]. Clinopyroxene grains ($n = 196$) recovered from Central Victoria Island mineral concentrates yield an estimate for the thickness of the lithosphere beneath that region of 215 ± 30 km (Extended Data Fig. 3)[27].

Seismic modelling

We use the previously published tomographic model SL2013NA[12], which is a continental-scale three-dimensional tomographic model of the North

American continent, cast in a global context. This model is generated using automated multimode inversion[60], which computes waveform fits for individual seismograms, followed by a three-dimensional tomographic inversion for compressional and vertically polarized shear-wave velocity and azimuthal anisotropy[61,62]. The SL2013NA model is constructed from more than 700,000 successfully fitted vertical component seismograms on a target triangular grid with a global-average spacing of 250 km. As a result of performing waveform fits, the model combines information from fundamental and higher-mode Rayleigh-wave surface waves (which capture the direct and multiple-S body-wave arrivals), and therefore has very good resolving power in the upper mantle, down to depths of about 700 km. We compute the maximum lateral velocity gradient at 150 km and 200 km depth by computing the maximum uphill gradient within the study location. The gradient is plotted in % per 100 km; that is, 1% per 100 km means that the shear-wave velocity changes by 1% within 100 km of that location. Note that this captures only the magnitude of the velocity change, not the sense of the velocity change. The model of the depth of the lithosphere–asthenosphere boundary is computed from SL2013NA using a previously proposed method[47]. This method was developed for global seismic models and uses the age progression of the depth of the lithosphere–asthenosphere boundary in the oceans to calibrate the models. It results in a model for the lithosphere–asthenosphere boundary that dominantly reflects the seismic expression of the thermal lithosphere–asthenosphere boundary, although some variation for composition is carried out. We note that the relative depth of the lithosphere–asthenosphere boundary (that is, the pattern) is more robust than the absolute depth.

Numerical modelling

We use the finite-element code Citcom[63–65] to solve thermochemical flow with extended Boussinesq approximation[66,67]. A particle-tracking technique is used to track the movement of different chemical fields, including cratonic root and melt depletion. The detailed numerical method, including governing equations, rheology and mantle-plume setup, is provided elsewhere[17].

We further include melting of mantle rock and depletion-dependent buoyancy and strengthening in the model. An anhydrous melting parameterization[68] is used for plume melting. The amount of melting is calculated for each particle, and any melt generated is removed immediately, assuming instantaneous extraction to the surface. The depletion field is updated with accumulated melting degree with each particle, which is then advected with particles just as other chemical fields.

We apply an exponential change in mantle rock density due to melt depletion[69]: $\rho = \rho_0 \exp(\alpha_d D)$, where α is the rate of density change due to melt depletion D. A reference value of $\alpha_d = -0.0003$ is used, which leads to a density change 1.04% at a melt depletion of 35%.

A composite rheology of non-Newtonian and Newtonian viscosity is used, with consideration of composition-dependent effects. The strengthening factor due to composition and melt depletion is calculated as

$$\Delta\eta = \Delta\eta_0^{\min(1, C/C_\eta)},$$

where C is the composition field, including cratonic root and melt depletion and C_η is the composition threshold for maximum strengthening. We use a constant-strain-rate definition for $\Delta\eta$, which would lead to an increase in non-Newtonian viscosity by $\Delta\eta^n$ in the definition of constant stress[17]. For cratonic lithosphere, a strengthening factor of $\Delta\eta = 6$ is used to maintain its stability. For melt residue, we use a strengthening factor of $\Delta\eta = 1$ (that is, no strengthening due to melt depletion) in the reference model and vary $\Delta\eta$ between 1 and 3 in other models. The rate of density change α_d is varied between −0.0004 and 0 in our models, according to a reasonable estimate for depleted mantle lithosphere based on the geochemical data and previous geodynamical studies[17].

Model setup. The model domain is 1,980 km wide and 660 km deep. Two cratonic roots, each with a thickness of 200 km and a width of 792 km, are located at two sides of the model domain (Fig. 3, Extended Data Fig. 6). The thin spot between them is around 400 km wide, roughly mimicking the size of lithosphere proposed to have been destroyed between two cratons in the north Slave region. For the models in Extended Data Fig. 7, the model domain is extended to be 2,640 km wide and 660 km deep, to include thinner, non-cratonic lithosphere at both sides. The initial thermal ages of cratonic lithosphere and thin lithosphere are 400 Myr and 30 Myr, respectively. A no-slip boundary condition is used on the top boundary, whereas other boundaries have free-slip conditions. We use a total of 288 × 96 elements, with vertical mesh refinement at depths of roughly 60–270 km and horizontal refinement surrounding the thin-spot area. This provides a spatial resolution of 5.5 km× 4.6 km in this region. To track the composition field, about 1.3 million particles are used in the whole model domain, resulting in an average particle density of around 47 particles per element.

The reference model was run for 50 Myr to a quasi-steady-state thermal field and then the model was restarted with different depletion buoyancy and strengthening. A hot plume with maximum temperature anomaly of 350 °C rises up from the bottom 660 km depth and hits the thin spot between two cratons. Figure 3 shows how buoyant plume residue fills the thin spot and leads to the growth (thickening) of the lithosphere between the two cratons. Supplementary Videos 1 and 2 show the evolution of temperature, depletion and viscosity field through time.

Extended Data Fig. 6 shows the result of models with different depletion buoyancy and strengthening at around 400 Myr. The importance of depletion buoyancy of the plume residue can be seen from the comparison between models R, B1, B2 and B3. The thin spot between cratons can be filled and thickened to about 200 km under conditions of sufficient melt-depletion-induced buoyancy alone (models R and B3). This is consistent with the high level of melt depletion in the Artemisia peridotites, as indicated by their low Al_2O_3 contents. With the additional aid of melt-depletion strengthening, plume residues can heal the thin spot with less depletion buoyancy (model V1). The composition field of the cratonic root shows that the surrounding cratonic root can be partially involved, by entrainment, in the formation of the new thick lithosphere. Extended Data Fig. 7 illustrates that the proposed mechanism of plume recratonization can lead to the growth of cratonic lithosphere in a more general situation, whether the plume is underneath or about 1,000 km away from the lithospheric thin spot between the two cratons. In addition, we provide a quantitative analysis by monitoring the thickness evolution of the lithospheric thin spot, mainly as a function of the rate of density change and of viscosity strengthening (Extended Data Fig. 8). Modelling results demonstrate that, without any viscosity strengthening, the lithosphere thickness can grow to approximately 200 km with high depletion buoyancy in models R and B3. With slight viscosity strengthening, intermediate buoyancy can also fill and stabilize the thin spot to about 200 km.

Data availability

The data that support the findings of this study are available at https://doi.org/10.6084/m9.figshare.13789354. Source data are provided with this paper.

Code availability

The code for geodynamic modelling is available on reasonable request to the corresponding author.

48. Graham, I. et al. Exploration history and geology of the Diavik kimberlites, Lac de Gras, Northwest Territories, Canada. In *Proc. 7th International Kimberlite Conference* Vol. 1 (eds Gurney, J. J. et al.) 262–279 (Red Roof Design, 1999).

49. Heaman, L. M., Creaser, R. A. & Cookenboo, H. O. Extreme high-field-strength element enrichment in Jericho eclogite xenoliths: a cryptic record of Paleoproterozoic subduction, partial melting and metasomatism beneath the Slave craton, Canada. *Geology* **30**, 507–510 (2002).
50. Armstrong, J. P., Fitzgerald, C. E., Kjarsgaard, B. A., Heaman, L. & Tappe, S. Kimberlites of the Coronation Gulf field, northern Slave craton, Nunanvut Canada. In *10th International Kimberlite Conference, Extended Abstracts* abstr. 10IKC-170 (2012); https://doi.org/10.29173/ikc3723.
51. Heaman, L. M., Kjarsgaard, B. A. & Creaser, R. A. The timing of kimberlite magmatism in North America: implications for global kimberlite genesis and diamond exploration. *Lithos* **71**, 153–184 (2003).
52. Kopylova, M. G. & Russell, J. K. Chemical stratification of cratonic lithosphere: constraints from the Northern Slave craton, Canada. *Earth Planet. Sci. Lett.* **181**, 71–87 (2000).
53. Boyd, F. R. & Mertzman, S. A. in *Magmatic Processes: Physicochemical Principles* (ed. Mysen, B. O.) 13–24 (Geochemical Society, 1987).
54. Ottley, C. J., Pearson, D. G. & Irvine, G. J. in *Plasma Source Mass Spectrometry: Applications and Emerging Technologies* (eds Holland, J. G. & Tanner, S. D.) 221–230 (Royal Society of Chemistry, 2003).
55. Harris, G. A. et al. Mantle composition, age and geotherm beneath the Darby kimberlite field, west central Rae Craton. *Mineral. Petrol.* **112**, 57–70 (2018).
56. Pearson, D. G. & Woodland, S. J. Solvent extraction/anion exchange separation and determination of PGEs (Os, Ir, Pt, Pd, Ru) and Re-Os isotopes in geological samples by isotope dilution ICP-MS. *Chem. Geol.* **165**, 87–107 (2000).
57. Liu, J. & Pearson, D. G. Rapid, precise and accurate Os isotope ratio measurements of nanogram to sub-nanogram amounts using multiple Faraday collectors and amplifiers equipped with 1012 Ω resistors by N-TIMS. *Chem. Geol.* **363**, 301–311 (2014).
58. Luguet, A., Nowell, G. M. & Pearson, D. G. Os-184/Os-188 and Os-186/Os-188 measurements by negative thermal ionisation mass spectrometry (N-TIMS): effects of interfering element and mass fractionation corrections on data accuracy and precision. *Chem. Geol.* **248**, 342–362 (2008).
59. Grütter, H. S. Pyroxene xenocryst geotherms: techniques and application. *Lithos* **112** (Suppl. 2) 1167–1178 (2009).
60. Lebedev, S., Nolet, G., Meier, T. & Van Der Hilst, R. D. Automated multimode inversion of surface and S waveforms. *Geophys. J. Int.* **162**, 951–964 (2005).
61. Lebedev, S. & Van Der Hilst, R. D. Global upper-mantle tomography with the automated multimode inversion of surface and S-wave forms. *Geophys. J. Int.* **173**, 505–518 (2008).
62. Schaeffer, A. J. & Lebedev, S. Global shear speed structure of the upper mantle and transition zone. *Geophys. J. Int.* **194**, 417–449 (2013).
63. Moresi, L. N. & Solomatov, V. S. Numerical investigation of 2D convection with extremely large viscosity variations. *Phys. Fluids* **7**, 2154–2162 (1995).
64. Zhong, S., Zuber, M. T., Moresi, L. & Gurnis, M. Role of temperature-dependent viscosity and surface plates in spherical shell models of mantle convection. *J. Geophys. Res. Solid Earth* **105**, 11063–11082 (2000).
65. van Hunen, J., Zhong, S., Shapiro, N. M. & Ritzwoller, M. H. New evidence for dislocation creep from 3-D geodynamic modeling of the Pacific upper mantle structure. *Earth Planet. Sci. Lett.* **238**, 146–155 (2005).
66. Christensen, U. R. & Yuen, D. A. Layered convection induced by phase transitions. *J. Geophys. Res. Solid Earth* **90**, 10291–10300 (1985).
67. King, S. D. et al. A community benchmark for 2-D Cartesian compressible convection in the Earth's mantle. *Geophys. J. Int.* **180**, 73–87 (2010).
68. Katz, R. F., Spiegelman, M. & Langmuir, C. H. A new parameterization of hydrous mantle melting. *Geochem. Geophys. Geosyst.* **4**, 1073 (2003).
69. Schutt, D. L. & Lesher, C. E. Effects of melt depletion on the density and seismic velocity of garnet and spinel lherzolite. *J. Geophys. Res. Solid Earth* **111**, B05401 (2006).
70. Kennedy, C. S. & Kennedy, G. C. The equilibrium boundary between graphite and diamond. *J. Geophys. Res.* **81**, 2467–2470 (1976).
71. Day, H. W. A revised diamond-graphite transition curve. *Am. Mineral.* **97**, 52–62 (2012).
72. McDonough, W. F. & Sun, S. S. The Composition of the Earth. *Chem. Geol.* **120**, 223–253 (1995).
73. Heaman, L. M., LeCheminant, A. N. & Rainbird, R. H. Nature and timing of Franklin igneous events, Canada: implications for a Late Proterozoic mantle plume and the break-up of Laurentia. *Earth Planet. Sci. Lett.* **109**, 117–131 (1992).
74. Mackinder, A., Cousens, B. L., Ernst, R. E. & Chamberlain, K. R. Geochemical, isotopic, and U–Pb zircon study of the central and southern portions of the 780 Ma Gunbarrel Large Igneous Province in western Laurentia. *Can. J. Earth Sci.* **56**, 738–755 (2019).
75. Wingate, M., Pirajno, F. & Morris, P. Warakurna large igneous province: a new Mesoproterozoic large igneous province in west-central Australia. *Geology* **32**, 105–108 (2004).
76. Fishwick, S. & Reading, A. M. Anomalous lithosphere beneath the Proterozoic of western and central Australia: a record of continental collision and intraplate deformation? Precambr. *Res.* **166**, 111–121 (2008).
77. Rudnick, R. & Nyblade, A. A. The thickness and heat production of Archean lithosphere, constraints from xenolith thermobarometry and surface heat flow. *Geochem. Soc. Spec. Publ.* **6**, 3–12 (1999).
78. Pidgeon, R. T. & Cook, T. J. F. 1214 ± 5 Ma dyke from the Darling Range, southwestern Yilgarn Craton, Western Australia. *Aust. J. Earth Sci.* **50**, 769–773 (2003).
79. Wang, X.-C., Li, Z.-X., Li, J., Pisarevsky, S. A. & Wingate, M. T. D. Genesis of the 1.21 Ga Marnda Moorn large igneous province by plume–lithosphere interaction. *Precambr. Res.* **241**, 85–103 (2014).
80. Geissler, W., Sodoudi, F. & Kind, R. Thickness of the Central and Eastern European lithosphere as seen by S receiver functions. *Geophys. J. Int.* **181**, 604–634 (2010).
81. Puchkov, V. et al. The ca. 1380 Ma Mashak igneous event of the Southern Urals. *Lithos* **174**, 109–124 (2013).
82. Stark, J. C. et al. 1.39 Ga mafic dyke swarm in southwestern Yilgarn Craton marks Nuna to Rodinia transition in the West Australian Craton. *Precambr. Res.* **316**, 291–304 (2018).
83. Youbi, N. et al. The 1750Ma Magmatic Event of the West African Craton (Anti-Atlas, Morocco). *Precambr. Res.* **236**, 106–123 (2013).
84. Jessell, M., Begg, G. & Miller, M. The geophysical signatures of the West African Craton. *Precambr. Res.* **274**, 3–24 (2016).
85. Feng, M., van der Lee, S. & Assumpção, M. Upper mantle structure of South America from joint inversion of waveforms and fundamental mode group velocities of Rayleigh waves. *J. Geophys. Res. Solid Earth* **112**, B04312 (2007).
86. Reis, N. J. et al. Avanavero mafic magmatism, a late Paleoproterozoic LIP in the Guiana Shield, Amazonian Craton: U–Pb ID-TIMS baddeleyite, geochemical and paleomagnetic evidence. *Lithos* **174**, 175–195 (2013).
87. French, J. E., Heaman, L. M., Chacko, T. & Srivastava, R. K. 1891–1883Ma Southern Bastar–Cuddapah mafic igneous events, India: a newly recognized large igneous province. *Precambr. Res.* **160**, 308–322 (2008).
88. Maurya, S. et al. Imaging the lithospheric structure beneath the Indian continent. *J. Geophys. Res. Solid Earth* **121**, 7450–7468 (2016).
89. Shellnutt, J. G., Hari, K. R., Liao, A. C. Y., Denyszyn, S. W. & Vishwakarma, N. A. 1.88 Ga giant radiating mafic dyke swarm across southern India and Western Australia. *Precambr. Res.* **308**, 58–74 (2018).

Acknowledgements We thank J. Li, Y. Sun, Y. Xu, Y. Luo, R. Cai, K. Zong, S. Woodland, G. Nowell, S. Jackson and C. Sarkar for help with analytical matters. This research was financially supported by the National Natural Science Foundation of China (41822301, 41790451, 41730214), China "1000 Youth Talents Program" and the 111 project (B18048) to J.L., by the Geomapping for Energy & Minerals program (Diamond project) of the Geological Survey of Canada (B.A.K. and D.G.P.) and the Canada Excellence Research Chairs program to D.G.P., and by the National Key R&D Program of China (2019YFA0708400, 2020YFA0714800 and 2019YFC0605403). This is GSC contribution number 20200737 and CUGB petrogeochemical contribution number PGC20150068 (RIG-no. 9).

Author contributions D.G.P., J.L. and B.A.K. conceived and designed the study. J.L., D.G.P. and B.A.K. wrote the manuscript and contributed to data interpretation. J.L., K.A.M., G.J.I. and B.A.K. conducted the analyses and data reduction. L.H.W performed numerical modelling. A.J.S. conducted the seismic modelling. All authors contributed to interpreting the data and writing the paper.

Competing interests The authors declare no competing interests.

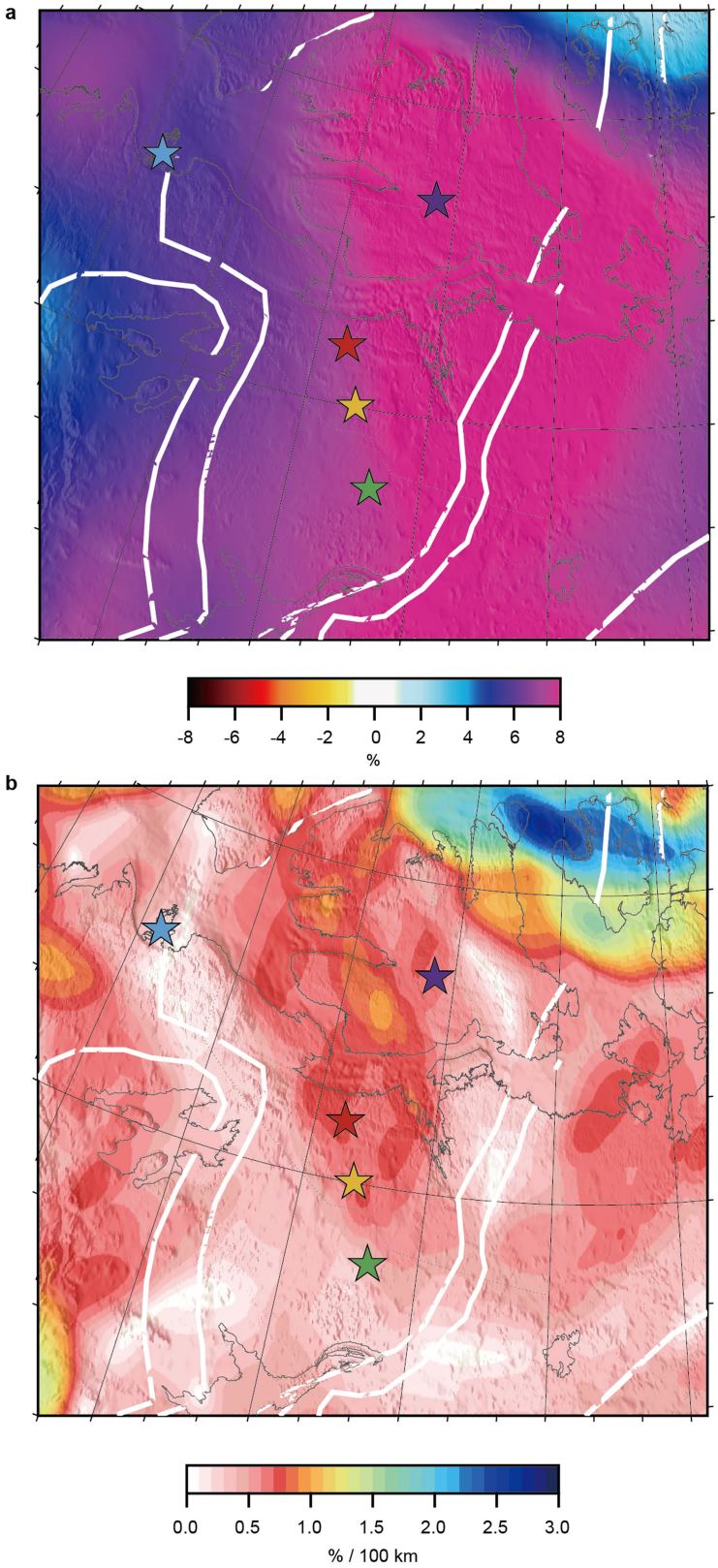
Additional information

Supplementary information The online version contains supplementary material available at https://doi.org/10.1038/s41586-021-03395-5.

Correspondence and requests for materials should be addressed to J.L.

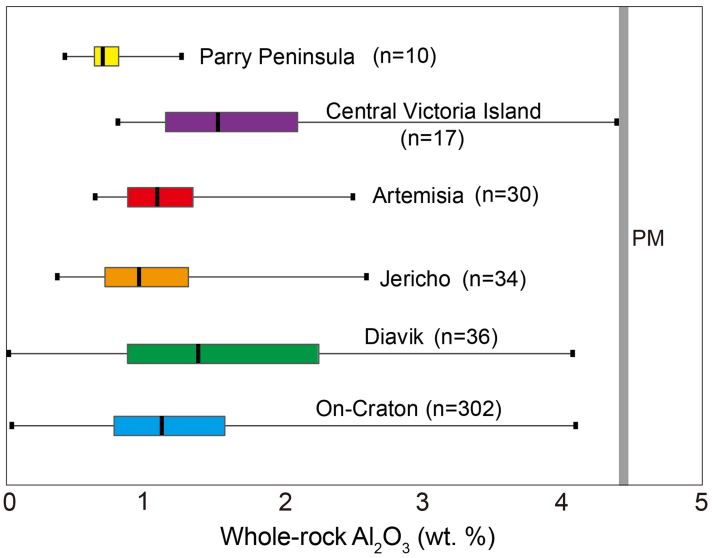
Peer review information *Nature* thanks Stephen Foley and the other, anonymous, reviewer(s) for their contribution to the peer review of this work. Peer reviewer reports are available.

Reprints and permissions information is available at http://www.nature.com/reprints.

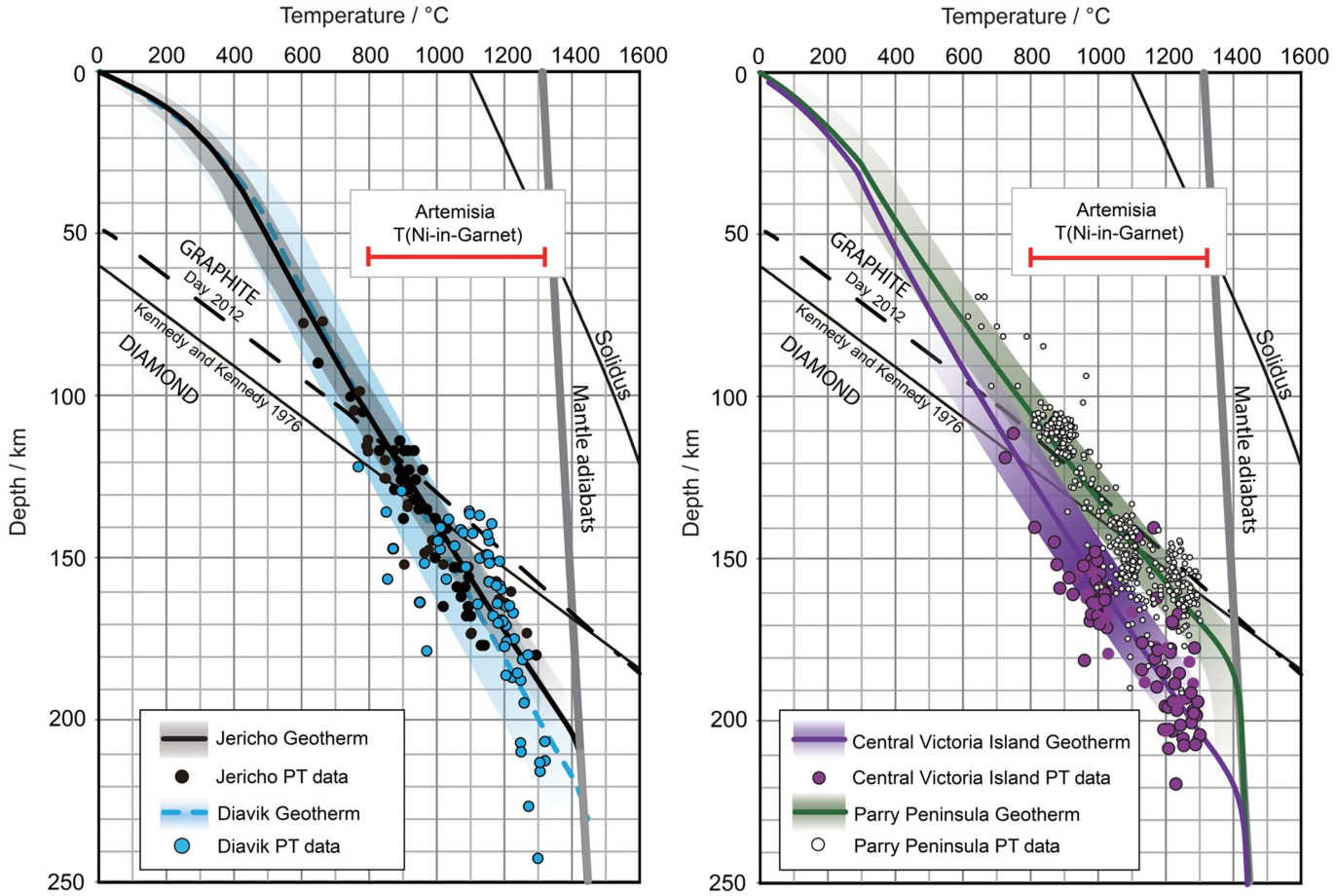


Extended Data Fig. 1 | See next page for caption.

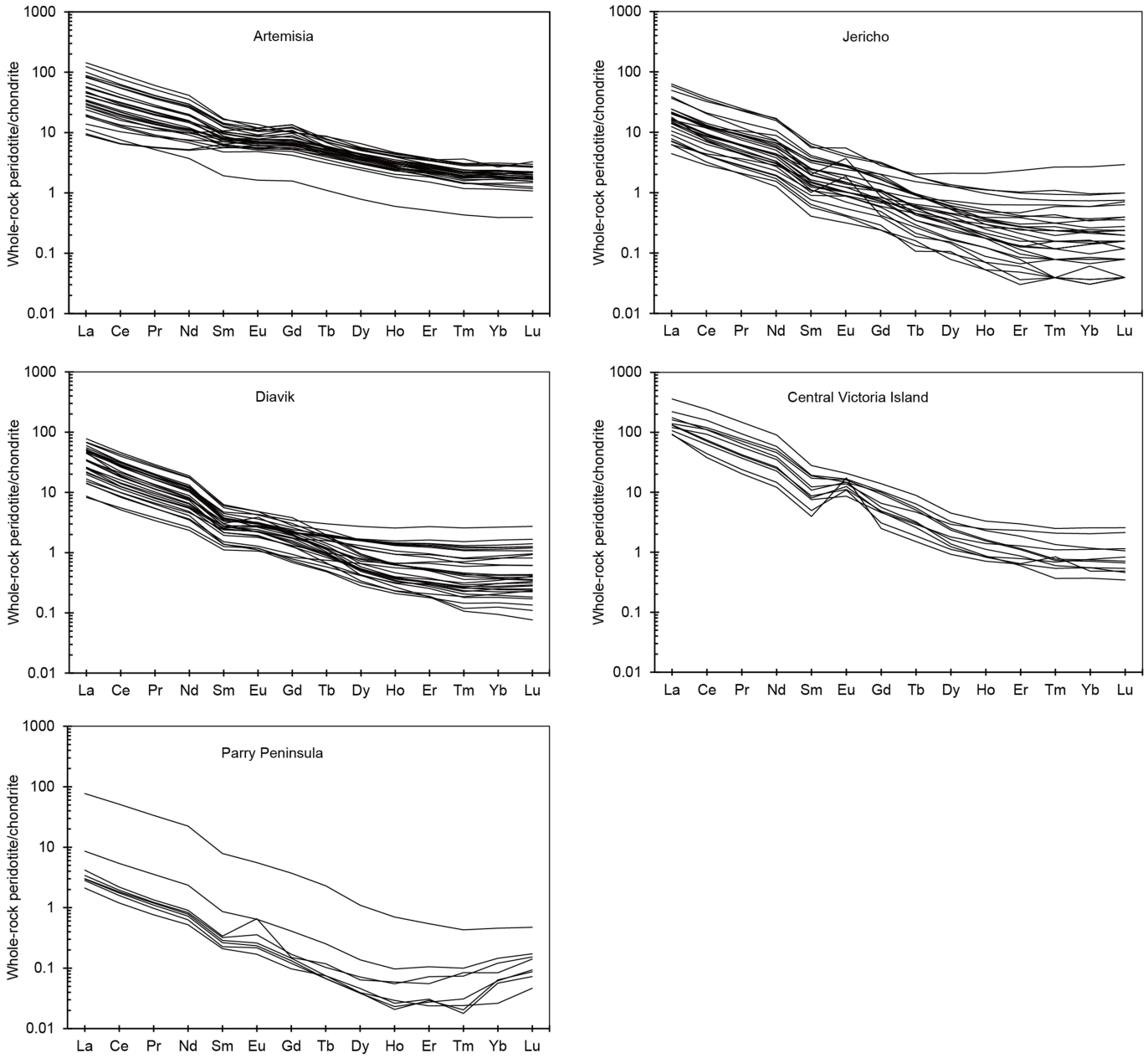
Extended Data Fig. 1 | Characteristics of seismic velocity in the Slave craton and surrounding areas. a, Map of seismic velocity from SL2013NA[12] at 150 km depth, shown as the percentage variation from the reference velocity of 4.39 km s^{-1} (colour scale). Because this location is in the middle of the stable cratonic shield, the velocities are dominated by positive perturbations, indicative of the colder and stronger cratonic mantle lithosphere. **b**, Map of the maximum lateral gradient in seismic velocity from SL2013NA[12] at 150 km depth, shown as the percentage variation in velocity per 100 km laterally (colour scale). Because this location is in the middle of the stable cratonic shield, the gradients in velocity are lower than at the craton margins or in actively deforming regions. The highest gradients are associated with the northern boundary of the stable cratonic mantle lithosphere north of Victoria Island. A small but non-zero gradient in velocity is observed trending north–northwest from Jericho–Artemisia through western Victoria Island, largely coincident with the main strike of the Mackenzie dyke swarm. Artemisia lies in a region with shorter-scale lateral variations, which suggests that it could have a slightly more fertile composition (as shown by the slightly lower median whole-rock Mg content of 90.4 versus 91.0; Supplementary Table 1) than other Slave localities. White lines in **a** and **b** denote the boundaries of the Archaean and Palaeoproterozoic tectonic domains (as in Fig. 1); kimberlite pipes are indicated as in Fig. 1a (stars).



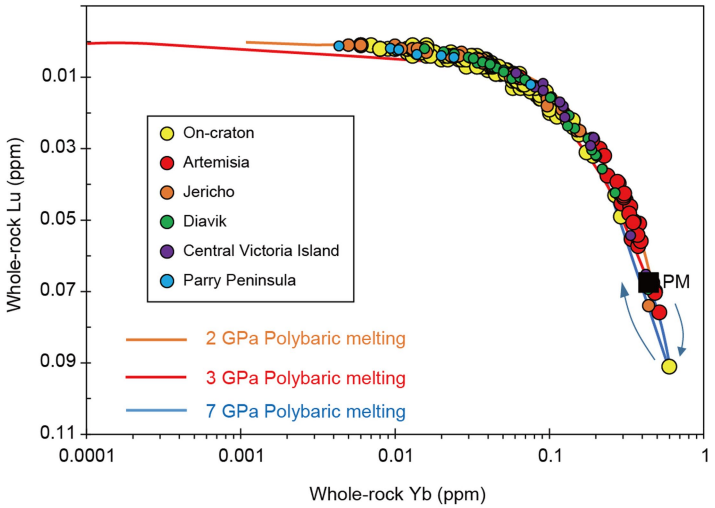
Extended Data Fig. 2 | Box-and-whisker plot of anhydrous whole-rock Al_2O_3 content of Slave-craton peridotites. Data are provided in Supplementary Table 1. Global on-craton peridotite data are from the literature[22]. PM, primitive mantle.



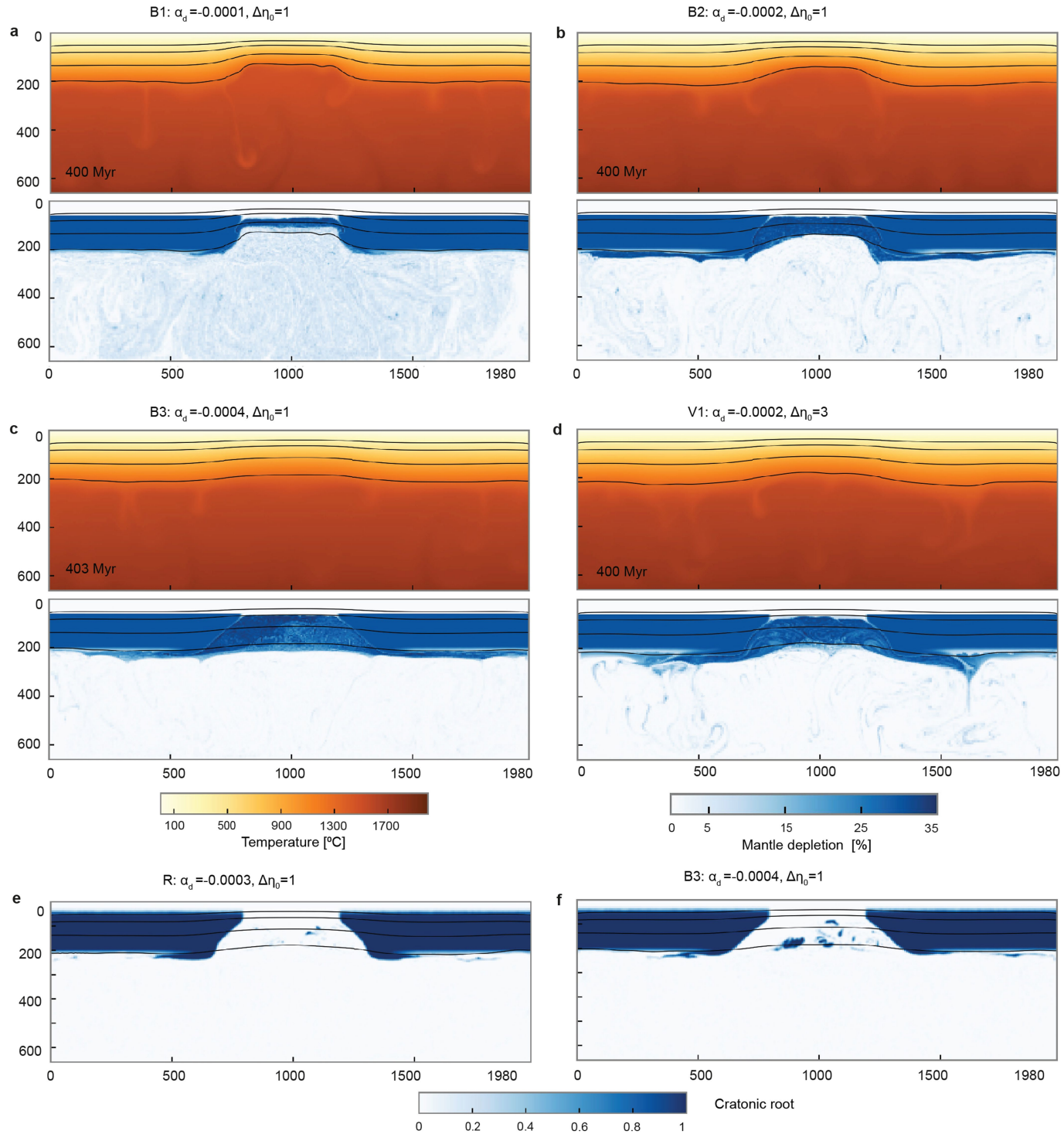
Extended Data Fig. 3 | Palaeogeotherms. Calculated clinopyroxene thermobarometry pressure–temperature (PT) data from xenoliths and till concentrates of the Slave craton (Supplementary Table 6) are fitted to define a mantle geotherm (solid line, with shading representing the 2σ error envelope) using the FITPLOT (parameters are shown in Extended Data Table 2) method[32]. The left panel shows the cases for Diavik (n = 65) and Jericho (n = 39); the right panel shows those of Parry Peninsula (n = 362) and Central Victoria Island (n = 196) (data from ref. [27]). Despite no fresh pyroxene minerals to allow a pressure–temperature calculation in Artemisia, application of the Ni-in-garnet thermometer (Supplementary Table 5) defines the sampled range of lithospheric mantle depths when extrapolated to the palaeogeotherms from other Slave localities in light of the diamondiferous feature in these kimberlites; therefore, the lithosphere thickness beneath Artemisia may be assumed to be similar to that beneath the nearby Jericho. The diamond and graphite transitions from ref. [70] and ref. [71], respectively, are plotted for reference.



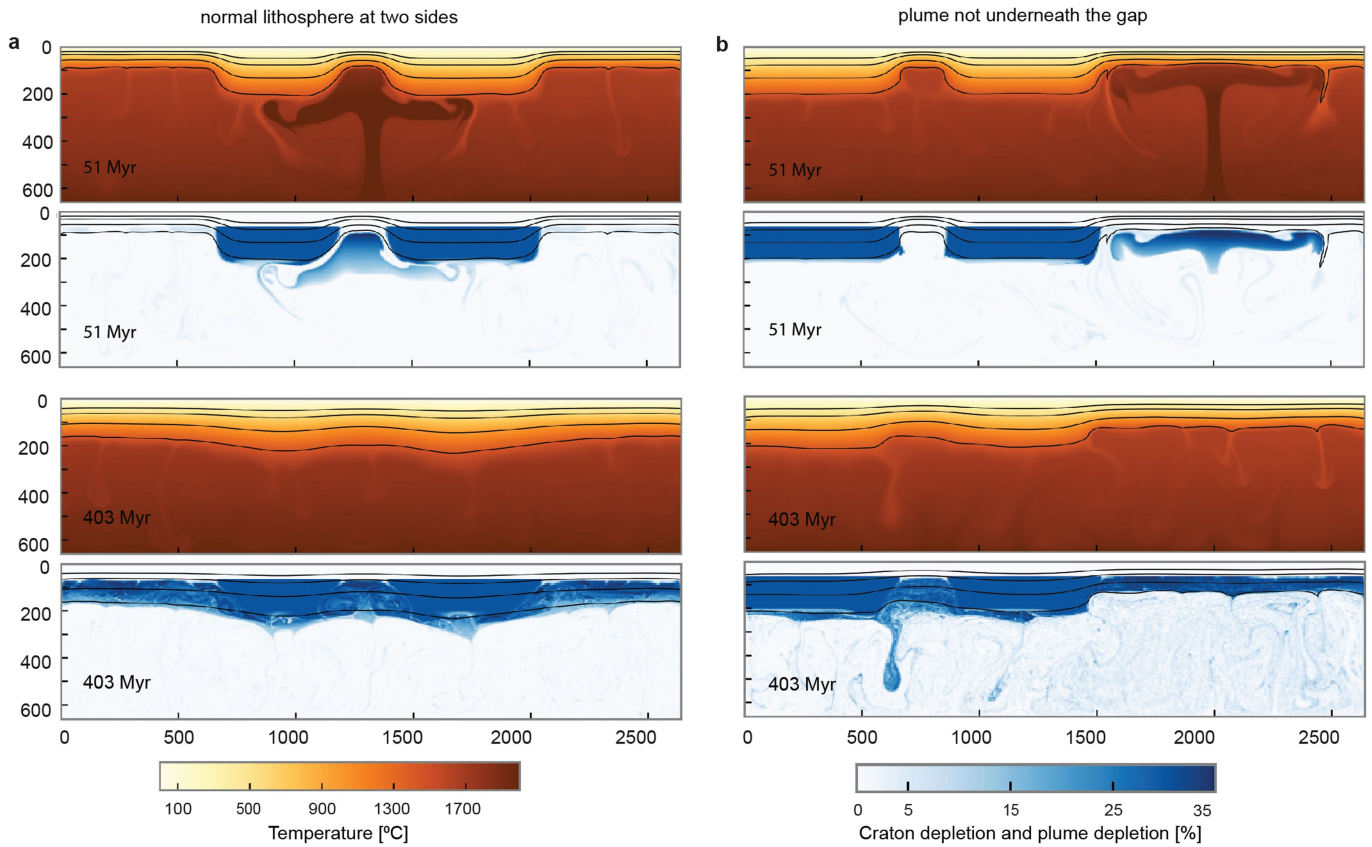
Extended Data Fig. 4 | Chondrite-normalized whole-rock rare-earth element patterns for Slave peridotites. Data are provided in Supplementary Table 1. All the Slave peridotites show enrichments of light to middle rare-earth elements relative to heavy rare-earth elements. The data for CI chondrites are from ref. [72].



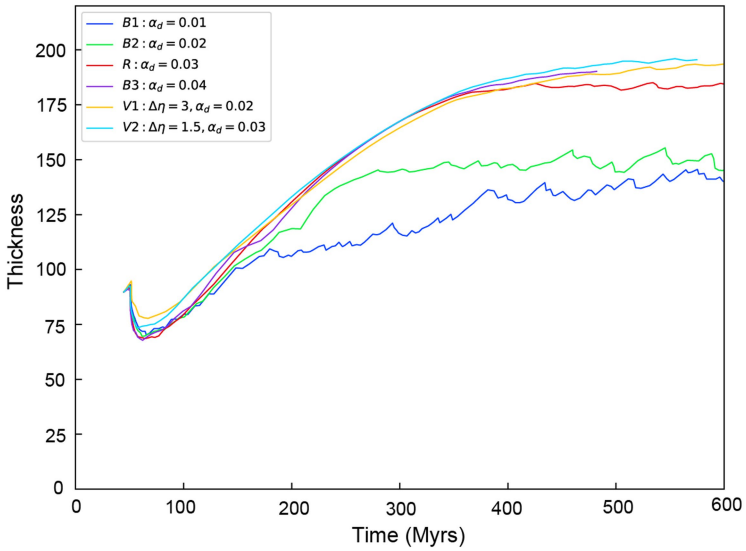
Extended Data Fig. 5 | Whole-rock Yb versus Lu content for Slave peridotites. Curves show the trajectories of residual mantle after polybaric fractional melting, beginning at 2 GPa (spinel facies; orange), 3 GPa (shallow garnet facies; red) and 7 GPa (deep garnet facies; blue). The partial melting calculations followed those in ref. [39], supplementary material C. Unlike all other reported cratonic peridotites, the very high Lu and Yb (heavy rare-earth element) abundances of Artemisia peridotites clearly indicate initial melting in the presence of high modal garnet, that is, ultradeep plume melting. The previously published data from the North Atlantic, Rae and Kaapvaal cratons[39] are plotted for comparison. PM, primitive mantle.



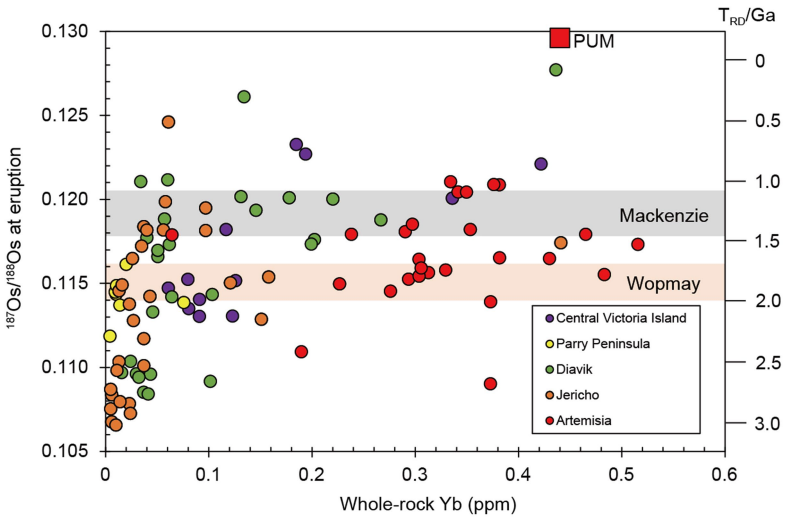
Extended Data Fig. 6 | Modelling with different depletion buoyancy and strengthening at around 400 Myr. a–**d**, Temperature and depletion field at around 400 Myr for models with different depletion buoyancy and strengthening (**a**, B1; **b**, B2; **c**, B3; **d**, V1). The depletion field is a combination of the compositional field of the cratonic root and melt depletion. Melt-induced depletion buoyancy of the plume residue has an important role and depends on α_d: the smaller α_d is, the more buoyant the plume residue becomes; $\Delta\eta$ is the viscosity strengthening factor due to melt depletion. **e**, **f**, The composition field of the cratonic root at around 400 Myr for models R (**e**) and B3 (**f**). The sequence shows that, within the parameters of the model, part of the cratonic root can be eroded by plume flow and then become involved in the formation of new lithosphere at the thin spot. Vertical and horizontal axes are in kilometres.



Extended Data Fig. 7 | Growth scenarios of cratonic lithosphere when a plume hits. a, Modelling an example with normal lithosphere at two side boundaries. **b**, Modelling an example with plume not under the thin spot between two cratons. The parameters for plume residue are $\alpha_d = -0.03\%$, $\Delta\eta = 3$ (**a**) and $\alpha_d = -0.02\%$, $\Delta\eta = 1$ (**b**). These two examples show that the proposed mechanism can lead to the growth of cratonic lithosphere in more general situations. Vertical and horizontal axes are in kilometres.



Extended Data Fig. 8 | Thickness evolution of the thin spot between two cratons as defined by the 1,300 °C isotherm. Without any viscosity strengthening, the lithosphere thickness may grow to approximately 200 km with high depletion buoyancy in models R and B3. With slight viscosity strengthening, intermediate buoyancy may also fill and stabilize the thin spot to around 200 km.



Extended Data Fig. 9 | Relationship between whole-rock Yb content and $^{187}Os/^{188}Os$ calculated at the time of kimberlite eruption or T_{RD} eruption. Data are provided in Supplementary Table 1. PUM, primitive upper mantle.

Extended Data Table 1 | Summary of major Proterozoic large igneous provinces and their impact on cratons

LIPs*	Location	Age	Present-day lithosphere thickness#	Ref.§
Frankin	Across northern Canada shield	0.72 Ga	~200 km	10,73
Gunbarrel	Western Laurentian Craton	0.78 Ga	~140-200 km	10,74
Warakurna	West-central Australian Craton	1.07 Ga	150-200 km	75,76
Umkondo & Laurentian	Kalahari and Laurentia Cratons	1.11 Ga	~200-250 km	8,77
Marnda Moorn	Yilgarn Craton	1.21 Ga	~200 km	76,78,79
Mackenzie	Northern Slave Craton	1.27 Ga	~200 km	This study
Mashak	Eastern margin of the East European Craton	1.38 Ga	180-200 km	80,81
Biberkine	SW Yilgarn Craton	1.39 Ga	~200 km	76,82
Tagragra of Akka	West African Craton	1.75 Ga	~160-220 km	83,84
Avanavero	Northern Amazonian Craton	1.79 Ga	~150-200 km	85,86
Sonakhan	Bastar Craton	1.88 Ga	~140-200 km	87-89
Bushveld	Kaapvaal Craton	2.05 Ga	~200 km	7

*We compiled the major Proterozoic large igneous provinces (LIPs) and the present-day lithospheric thickness of cratons that were impacted by the plumes; more are provided in ref. [9].
#The present-day lithospheric thickness is determined by seismology and/or pressure–temperature geotherms of mantle xenolithic peridotites during Phanerozoic eruptions.
§Data from refs. [7–10,73–89], as indicated.

Extended Data Table 2 | FITPLOT parameters used for constructing palaeogeotherms

Parameters	Diavik	Jericho	Parry Peninsula	Central Victoria Island
Lower crust (km)	22	18	10	10
Upper crust (km)	23	17	18	18
Upper cust heat production (W/m^3)	1.12E-06	1.12E-06	1.12E-06	1.12E-06
Lower crust heat production (W/m^3)	4.00E-07	4.00E-07	4.00E-07	4.00E-07
Mantle heat production (W/m^3)	4.00E-09	0	0	0
Lithosphere thickness (km)	217±21	203±11	185±20	215±30
Estimated diamond window (km)	122-217	117-203	145-185	119-215